Magnetoelastic coupling at spin-glass-like transition in $Sr_3NiSb_2O_9$

A. Chatterjee[1], S. Majumdar[1], S. Chatterjee[2], A.-C. Dippel[3], O. Gutowski[3], M. V. Zimmermann[3], S. Giri[1]

[1] *Department of Solid State Physics, Indian Association for the Cultivation of Science, Jadavpur, Kolkata 700032, India*

[2] *UGC-DAE Consortium for Scientific Research, Kolkata Centre, Sector III, LB8, Salt Lake, Kolkata 700 098, India*

[3] *Deutsches Elektronen-Synchrotron, Notkestr. 85, 22607 Hamburg, Germany*

Abstract

We report a characteristic spin-glass-like behavior in $Sr_3NiSb_2O_9$, as confirmed from the low-field dc magnetometry and ac susceptibility measurements. The memory effects in the dc magnetometry exhibit similar characteristic features of the spin-glass systems. The ac susceptibility measurements provide that the frequency dependent peak-shift follows the conventional Vogel-Fulcher and dynamical scaling laws with the characteristic relaxation time to be $\sim 10^{-14}$ s. This relaxation time fits in the recommended range of $\sim 10^{-12} - 10^{-14}$ s for the classical spin-glasses. Low temperature synchrotron diffraction studies point to the strong magnetoelastic coupling close to the spin-glass-like transition. The transition is found to be associated with the step-like anomalous lattice contraction. Possible origin of magnetic frustration leading to the spin-glass ground state is discussed by correlating the microstructural results, as obtained from the analysis of synchrotron diffraction studies.

Keywords: `Magnetoelastic effect; structural properties; spin-glass`

Email address: `sspsg2@iacs.res.in` (S. Giri[1])

1. Introduction

Materials with spin-glass (SG) ground state are disordered magnetic materials, where spins residing on the lattice do not align in any ordered direction in long range order. The characteristics of SG state have been explored theoretically and experimentally in various kinds of systems [1, 2, 3, 4, 5, 6]. Theoretically, the SG models are fascinating for exciting analytical and numerical studies in computer physics [7, 8]. One of the difficult problems faced in computational physics is generating the equilibrium states of disordered systems with rough free-energy landscapes, as observed in classical spin-glasses. The disorder and magnetic frustration ascribed to the competing magnetic interactions are the primary reason for obtaining frozen SG state [6]. Any sets of spin interaction competes among themselves to minimize the energy. But when any kind of spin configuration cannot minimise all of the interactions simultaneously then it becomes frustrated system [9]. Magnetic frustrations classically occur due the competing ferromagnetic (FM) and antiferromagnetic (AFM) interactions. This can also appear in magnet due to antiferromagnetically coupled different geometric units formed by the magnetic ions such as two-dimensional triangular, kagomé, and three-dimensional pyrochlore lattices [10, 11]. The frustration may also emerge due to competing nearest-neighbor and next nearest-neighbor interactions. Over last few decades different aspects of SG state have been explored experimentally and theoretically in new systems by probing new techniques. Recently, the role of magnetoelastic consequence to the SG state has been focused in few occasions of theoretical[12, 13, 14] and experimental studies [15, 16, 17]. However, systematic studies of magnetoelastic coupling correlated to the SG transition are still lacking.

The compound, $Sr_3NiSb_2O_9$ belongs to the general formula of $A_2A'B_2B'O_9$ or $A(B_{2/3}B'_{1/3})O_3$ (considering A and A' as same cation). In case of $Sr_3NiSb_2O_9$ the B and B' are represented by the di-valent Ni^{2+} and penta-valent Sb^{5+} ions. Here, Ni^{2+} with $3d^8$ electronic configuration is magnetic. In Fig. 1 the compound crystallizes in a $P2_1/n$ space group. The crystal structure has two

crystallographically distinct octahedral sites with occupancies Sb (0.970), Ni (0.030) and Sb (0.363), Ni (0.637). The structure clearly demonstrates disordered occupancies of the magnetic Ni^{2+} ions. The results indicate that this candidate is a promising candidate for SG state, where disordered occupancies of Ni^{2+} is one of the crucial parameters. Magnetization results revealed a small increase of magnetization around $\sim$ 100 K, followed by an apparent peak around 8 K [18]. The high temperature anomaly was suggested due to appearance of ferrimagnetic clusters. The low temperature peak was speculated to be a consequence of a relaxor ferromagnetic behavior, which is also proposed in isostructural $La_3Ni_2SbO_9$[19] or proposed SG-like bahavior in isostructural $La_3Ni_2NbO_9$ [20].

In this paper we focus on the dc magnetization and ac susceptibility measurements for characterizing the low temperature peak around 8 K. The zero-field cooled (ZFC) and field-cooled (FC) memory effects below the low temperature peak confirm the SG-like state. In order to study the spin glass nature, ac susceptibility under different frequenciesis studied [21]. Frequency dependent shift of the low temperature peak, as obtained from the ac susceptibility measurements, satisfies the Vogel-Fulcher and dynamical scaling laws with results similar to that observed for the classical SG systems. In order to probe the probable magnetoelastic coupling correlated to the SG-like transition, the low temperature synchrotron diffraction studies are performed in range of 8$-$300 K. The results reveal a significant magnetoelastic coupling both at the high temperature anomaly and low temperature transition. We note that the SG-like transition is associated with the anomalous and anisotropic contraction of the unit cell volume, where contraction in the $a-b$ plane is much stronger than the contraction along c axis. Microscopic structural parameters are discussed correlated to the SG-like state in $Sr_3NiSb_2O_9$.

2. Experimental details

Polycrystalline $Sr_3NiSb_2O_9$ is prepared from the stoichiometric mixture of pelletised strontium carbonate, antimony (V) oxide, and nickel oxide using solid-state reaction [18]. The single phase chemical composition is confirmed by the x-ray diffraction studies at room temperature recorded in a PANalytical x-ray diffractometer (Model: X' Pert PRO) using Cu Kα radiation. The results are further confirmed by the synchrotron diffraction studies measured at beamline P07 at PETRA III, Hamburg, Germany at a wavelength of 0.14235 Å using a 2-D Perkin Elmer detector [22]. The synchrotron powder diffraction data are analyzed using Rietveld refinement with commercially available MAUD and FullProf softwares. The dc magnetization and ac susceptibility are measured in a commercial magnetometer of Quantum Design (MPMS, evercool), where dc magnetization is recorded in both the zero-field cooled (ZFC) and field-cooled (FC) protocols.

Determination of grain sizes and energy-dispersive X-ray spectroscopy (EDX) are done using transmission electron microscopy (TEM) of the JEOL JEM, 2100F. The morphology of the sample as obtained from the TEM is illustrated in Supplementary information (see Fig S1). Average grain size is found to be in the range 0.5 μm to 1 μm. The EDX analysis at two different random regions of the sample revealed that the stoichiometric proportion of Sr, Ni, and Sb in $Sr_3NiSb_2O_9$ is found to be 3.08:1:1.85, which is close to the nominal ratio as 3:1:2.

3. Experimental results and discussions

Magnetization results

Thermal variations of ZFC and FC magnetization curves recorded at 100 Oe are depicted in Fig. 2(a). In accordance with the previous report a peak-like structure in the ZFC curve is observed around $\sim$ 8 K (T_g), as further highlighted in the inset of the figure [18]. Inset of the figure exhibits that the ZFC curve does not show a typical well-defined peak. It, rather, shows a flat region

in between $\sim$ 6 and $\sim$ 10 K, providing an average value of 8 K. This unusual nature of the peak might be influenced by the structural transition occurred close to 10 K, as obtained from the synchrotron diffraction studies, which will be discussed later in details. The ZFC and FC curves deviate from each other below $\sim$ 225 K, at which a step-like small increase in both the ZFC and FC curves is observed. In the inset of Fig. 2(a) the FC curve exhibits a signature of T_g, below which it shows a sharp rise down to the lowest measured temperature. Nature of the FC curve does not exhibit typical manifestation of the SG-like behavior displaying broadened peak around transition temperature [4]. The curve rather shows a sharp increasing trend below $\sim$ 8 K, as typically observed for superparamagnetic behavior [23, 26, 24]. Similar behavior with steep increase of FC magnetization below the transition temperature was also observed for $Sr_2CoNb_{0.9}Ti_{0.1}O_6$, which has been characterised as a spin-glass like compound from the ac susceptibility measurements and memory effect studies of dc magnetization [25]. In order to distinguish between superparamagnetic and spin-glass transition, the detailed ac susceptibility measurements by varying frequency and memory effect in the dc magnetization are performed in the current investigation, which is discussed below. Magnetic hysteresis loops are recorded at different temperatures. Loops at selective temperatures below and above T_g are depicted in Fig. 2(b). Central portion of the loop at 2 K is highlighted in the inset of Fig. 2(b). Here, the curve at 2 K does not show any saturating trend at 50 kOe. Reasonably large coercivity (H_C) of $\sim$ 980 Oe is observed at 2 K, which decreases considerably to 56 Oe at 6 K. The H_C nearly vanishes at 10 K. Magnetization curve is exactly linear above 25 K.

Memory effect

In order to characterize spin-glass transition, the experiment on memory effect has been carried out in different protocols [27, 28, 29, 30]. One of the protocols is summarized in Fig. 3(a). Sample is cooled from 40 K ($>> T_g$) down to 5 K in 100 Oe, waited for 3760 s in zero-field, and further cooling is done down to 2 K in 100 Oe. The cooling curve is shown by the blue curve

with square symbols. After settling the temperature at 2 K, sample is heated up at a heating rate of 1.0 K/min continuously in 100 Oe and the magnetization is recorded, as depicted by the red curve with filled circles in the figure. The reference FC curve is shown by the green curve with unfilled circles with a dot at the center. All the curves are depicted in Fig. 3(b). Encircled region of the curves in the figure is further highlighted in the inset of the figure. The FC heating curve clearly depicts a step-like feature around 5 K, at which sample-temperature is kept fixed during cooling procedure for 3760 s in zero-field. The evident signature in the FC heating curve around 5 K confirms the memory effect, which is typical, as observed in the frozen SG state [4]. In order to confirm memory effect similar experiment is performed in the ZFC protocol, as described in Fig. 4(a). The ZFC protocol is identical to the FC protocol, except for cooling process, where cooling is done in zero-field. Only magnetic field of 100 Oe is applied during magnetization measurement in the heating cycle. The ZFC curve is considered as the reference curve, which is shown together with the ZFC heating curve in Fig. 4(b). The difference between these two curves, defined as ΔM as a function of temperature, is plotted in Fig. 4(c). The difference plot exhibits a sharp 'dip' at 5 K, where sample-temperature is kept fixed for 3760 s during cooling process. The 'dip' confirms that in the continuous heating process it can retrieve the information of waiting sequence during cooling process and confirms the memory effect.

The memory experiment is further carried out in the relaxation dynamics, which is also described in Fig. 4(d). Here, sample is first cooled down to 6 K from 40 K in a 100 Oe magnetic field. After stabilizing the temperature at 6 K magnetic field is cut off and relaxation dynamics are recorded. The relaxation dynamics are measured by recording magnetization with time (t) for t_1 period, as depicted in Fig. 4(e). After t_1, sample-temperature is cooled down to 3 K and further relaxation is recorded for t_2 period after stabilizing the temperature at 3 K. After finishing the measurement for t_2, sample-temperature is returned back to 6 K and relaxation is recorded again for t_3. As shown in Fig. 4(f), the relaxation dynamics follow a single functional dependence when it is plotted for

$t_1 + t_3$ time period. The results clearly demonstrate that relaxation process in the beginning of measurement for t_3 retains previous history of the state at the end of t_1. This indicates that intermediate changes in condition by decreasing temperature do not alter the relaxation mechanism. Rather, it memorizes the previous history. The memory effect can be interpreted by the droplet model. For droplet model, droplet is defined as the lowest-energy excitation with length scale, D [31]. According to the model the magnetic domain grows during the waiting period at a particular temperature and it continues to grow if the domain size is smaller than D even at another temperature. If size becomes larger than D, the growth process restarts from the state with size D and can not restore the memory. As described in the Fig. 4(e), during intermediate relaxation process for t_2 period at 3 K the domain grows a little ($<$ D), such that it cannot exceed D and the growth process is restored. The memory effects in the thermal variations under both the ZFC and FC protocols as well as relaxation dynamics confirm the cooperative spin-spin correlation process, as observed for classical spin-glasses [4].

AC susceptibility

The ac susceptibility (χ_{ac}) measurements are performed at different frequencies (f) in the low temperature region around T_g. The real component (χ') of χ_{ac} with T is depicted in Fig. 5(a). Unlike ZFC curve, the $\chi'(T)$ exhibits a well-defined peak. A peak is observed at $\sim$ 8.8 K for the lowest-f measurement at 5.0 Hz. The peak is slightly higher than T_g ($\sim$ 8 K), as observed in the ZFC magnetization curve. The peak position in $\chi'(T)$ shifts toward higher temperature with increasing f. The f dependent shift shows it has spin glass like nature of transition [32, 33]. By taking into account $\omega = 2\pi f$, the values of $\Delta T_g/[T_g \Delta(\log \omega)]$ is found to be $\sim$ 0.01, which is close to the higher end in the range 0.005$-$0.010, as recommended for RKKY SGs [4]. The f dependent shift is usually analyzed using Vogel-Fulcher law as

$$\tau = \tau_0 \exp[E_a/k_B(T - T_0)], \tag{1}$$

Table 1: Structural parameters of $Sr_3NiSb_2O_9$ as obtained from the Rietveld refinement of the synchrotron diffraction data at 300 K.

Space group		*a (Å)*	*b (Å)*	*c (Å)*	Angle (degree)
$P2_1/n$		5.6399(9)	5.6405(2)	7.9615(0)	$\alpha = \gamma = 90$, $\beta = 90.31$
Atoms	Wyckoff		*x*	*y*	*z*	Occupancy
Sr	4e		0.49136(4)	0.51451(4)	0.23181(9)	1.0
Ni1/Sb1	2c		0	0.5	0	0.030/0.970
Ni2/Sb2	2d		0.5	0	0	0.637/0.363
O1	4e		0.77289(7)	0.75794(4)	-0.02799(9)	1.0
O2	4e		0.726(0)	0.271(0)	-0.039(0)	1.0
O3	4e		0.54083(5)	0.00272(7)	0.242(0)	1.0

Bond lengths

	Ni1-O	Ni2-O
O1	1.9504(0)	2.0703(7)
O2	2.0366(1)	2.0153(0)
O3	2.0553(6)	1.9272(8)

Bond angles

Ni1-O1-Ni2	Ni1-O2-Ni2	Ni1-O3-Ni2			
165.4(1)	159.6(4)	176.3(7)			
O1-Ni1-O2	O1-Ni1-O3	O2-Ni1-O3	O1-Ni2-O2	O1-Ni2-O3	O2-Ni2-O3
92.3(8)	91.7(9)	86.1(2)	89.2(8)	91.5(9)	85.6(8)

where τ_0 being the characteristic relaxation time, E_a is the anisotropy energy barrier, T_0 is a phenomenological parameter, and τ is the inverse of measuring frequency $(1/2\pi f)$. A good fit using Vogel-Fulcher law is shown in Fig. 5(b) by the straight line. The fit gives $T_0 \approx 7.99$ K and $\tau_0 \approx 0.3 \times 10^{-13}$ s. The f dependent shift is further fitted with the dynamical scaling law as

$$\tau_{max} = \tau_0' \zeta^{z\nu}. \tag{2}$$

Where $\zeta = T_0'/(T - T_0')$ is the correlation length, τ_0' is the microscopic flipping time, z is the dynamic exponent, ν is the spin-correlation length exponent, and T_0' provides the dc value for $f = 0$ (T_g). The satisfactory fit using dynamical scaling law is depicted in Fig. 5(c) by the straight line. Here, $T_0' \approx 8.5$ K, $\tau_0 \approx 0.1 \times 10^{-13}$ s, and $z\nu \approx 8.2$, are obtained from fit using Eq. (2). The results indicate that the parameters as obtained from both the Vogel-Fulcher and the dynamical scaling laws, fit well with the parameters recommended for classical SG systems [4]. We note that the values of T_0 and T_0' are 7.99 and 8.50 K, respectively, which are close to $T_g = 8.0$ K, as obtained from the low-field dc magnetization study. The values of τ_0 and τ_0' are $\sim 0.3 \times 10^{-13}$ and $\sim 0.1 \times 10^{-13}$ s, respectively, which exist in the range $\sim 10^{-12} - 10^{-14}$ s, as proposed for SGs [6]. The value of $z\nu \approx 8.2$ is also within the recommended range of 4−12, found for SGs [6]. The value of τ_0 is found to be 10^{-11} which is near about the recommended range [21].

Magnetoelastic coupling

In order to investigate structural correlation to the magnetization results, the structural properties are investigated by the x-ray powder diffraction studies using synchrotron source over a temperature range of 8.3−300 K. Here, 8.3 K is the lowest temperature, which could be achieved using our cryogen-free cryostat. Rietveld refinement of the diffraction pattern is done using $P2_1/n$ space group in the whole temperature range, as recommended in the previous report [18]. Example of two diffraction patterns together with the refinement using $P2_1/n$ space group at 300 and 8.3 K are shown in Figs. 6(a) and 6(b), respectively.

Inset of Figs. 6(a) demonstrates close view of a portion of the diffraction pattern at 300 K. The positional coordinates and lattice constants are listed in Table 1. The values are consistent with the previous report [18]. The reasonable reliability parameters are $R_w(\%) \sim 3.43$ and 4.04, $R_{exp}(\%) \sim 2.11$ and 2.14, and $\sigma \sim 1.63$ and 1.80 for diffraction patterns at 300 and 8.3 K, respectively. The bars below the diffraction patterns provide the diffraction peak positions and the difference plots are shown at the bottom for all the refinements, as shown in Figs. 6(a) and 6(b) at 300 and 8.3 K, respectively. All possible values of bond lengths and bond angles at 300 K are also listed in Table 1. The structural parameters are consistent with the reported results [18]. Two kinds of Ni/Sb atoms with different occupancies are observed, which are described as Ni1/Sb1 and Ni2/Sb2 positioned at 2c and 2d sites, respectively. Three oxygens defined as O1, O2, and O3 occupy at the corners of the Ni/Sb octahedra positioned at 4e site, where O1 and O2 are the basal oxygen atoms and O3 occupies the apex of the octahedra.

Temperature variation of the integrated intensity of the (110) diffraction peak is depicted in Fig. 6(c). Thermal variation of the intensity plot exhibits a considerable increase with decreasing temperature from 300 K and becomes nearly temperature independent around $\sim$ 200 K. With further decreasing temperature it shows a maximum around $\sim$ 150 K, below which it decreases with decreasing temperature down to $\sim$ 20 K. Below $\sim$ 20 K the intensity shows an increase of intensity with further lowering temperature. In order to probe thermal variation of lattice constants, diffraction data is refined in the entire temperature range of 8.3$-$300 K using $p2_1/n$ space group. The refined lattice constants, a, b, c, and β with T are depicted in Figs. 6(d), 6(e), 6(f), and 6(g), respectively. The $a(T)$ and $b(T)$ change similarly with decreasing temperature. The $a(T)$ decreases with T from 300 K and the decreasing trend becomes faster below $\sim$ 225 K, around which an anomaly is noticed in the thermal variations of both the ZFC and FC magnetization curves. A sharp fall in $a(T)$ is observed below $\sim$ 10 K, which is close to T_g, providing another evident signature of magnetoelastic coupling. The β parameter sharply decreases toward 90^0 below 10 K.

On the contrary, the $c(T)$ increases sharply with decreasing temperature from 300 K. The increasing trend becomes slower below $\sim$ 250 K and a weak anomaly may be correlated around $\sim$ 225 K, at which ZFC and FC magnetization curves show a step-like small change. Thermal variation of the unit cell volume (V) is depicted in Fig. 6(h). The V parameters decreases with decreasing temperature, analogous to the thermal variations of a and b parameters. Inset of Fig. 6(h) highlights the low-T regions, showing a sharp fall below $\sim$ 10 K. We note that decrease of V from 10 K to 8.3 K is considerable as 0.01 %, displaying an anomalous contraction of unit cell volume.

All possible bond lengths are calculated from the refined parameters as a function of temperature, which are depicted in Figs. 7(a-d). Similar temperature dependence of Ni1$-$O1 and Ni2$-$O1 are observed as shown in Figs. 7(a) and 7(b), respectively. In fact, the Ni1$-$O2 and Ni2$-$O2 also exhibit similar dependence (not shown in the figure). The bond length decreases with decreasing temperature and decreasing slope becomes faster around $\sim$ 225 K, at which a step-like small increase is observed in ZFC and FC magnetization curves, pointing a magnetoelastic coupling. With further decreasing temperature an anomalous sharp fall in the bond length is observed below $\sim$ 10 K, around which maximum is observed in the ZFC curve. The sharp decrease below $\sim$ 10 K is represented for Ni1$-$O1 in the inset of Fig. 7(a). On the contrary, the Ni1$-$O3 and Ni2$-$O3 bond lengths increase sharply below 300 K and increasing trend becomes slower below $\sim$ 250 K, as depicted in Fig. 7(c) and 7(d). Both the bond lengths show a sharp rise below $\sim$ 10 K, as further highlighted in the inset of Fig. 7(c). Thus, thermal variations of Ni$-$O bond lengths points to distortions of (Ni1,Ni2)O_6 octahedra. The distortions for Ni1O_6 and Ni2O_6 are similar. The basal O1 and O2 move toward Ni atom, resulting in the sharp decrease of Ni$-$O bond lengths below $\sim$ 10 K. On the other hand, the apex O3 oxygen moves away from Ni atoms, as Ni$-$O3 bond length sharply increases below $\sim$ 10 K. The example of distortion in a NiO_6 octahedron is depicted in the inset of Fig. 7(d), where contraction in the basal oxygens and elongation along the apex oxygen are illustrated by the arrows in the figure.

Three bond angles in the Ni−O−Ni superexchange paths are possible such as Ni1−O1−Ni2, Ni1−O2−Ni2, and Ni1−O3−Ni2. Thermal variations of the bond angles are studied. Since thermal variations of Ni1−O1−Ni2 and Ni1−O2−Ni2 behave similarly, the Ni1−O1−Ni2 and Ni1−O3−Ni2 are shown with T in Figs. 7(e) and 7(f), respectively. Contrast behaviour of the bond angles is observed. The Ni1−O1−Ni2 bond angle decreases with decreasing temperature associated with the anomalous sharp fall below $\sim$ 10 K, as depicted in the inset of Fig. 7(e). Magnitude of Ni1−O3−Ni2 is nearly 10^0 larger than Ni1−O1−Ni2 angle and it continues to increase toward 180^0 with decreasing temperature associated with a change of slope around $\sim$ 225 K. A steep increase is noted below $\sim$ 10 K, as depicted in the inset of 7(f).

Discussion and conclusion

Current ac susceptibility and low-field dc magnetization results confirm a spin-glass-like transition around 8.3 K (T_g). It is understood that disorder and magnetic frustration are the two primary parameters for obtaining spin-glasses [4, 6]. Here, disorder in Ni occupancy at the 2c and 2d sites is a crucial parameter for the occurrence of spin-glass transition. The structural studies demonstrate a strong magnetoelastic coupling associated with the spin-glass transition. The estimation of bond length around T_g confirms a considerable distortion of NiO_6 octahedra. This distortion lead to the significant change in the Ni−Ni distance, where the Ni−Ni distance decreases in the $a-b$ plane and increases along c axis. The step-like changes in Ni−Ni distance are considerable, which are $\sim$ 0.007 % for a small change of temperature from 10 K to 8.3 K. The arrangements of Ni atoms along different directions are depicted in Figs. 8(a), 8(b), and 8(c). Figure 8(a) illustrates nearly square lattice arrangements, whereas it forms isosceles triangles while projected along c axis, as depicted in Fig. 8(b). The antiferromagnetically coupled edge sharing isosceles triangles carry necessary ingredient for the topological magnetic frustration [10, 35, 36]. The AFM super-exchange interaction, as proposed in the reported results [18],

is significant in this context for $Sr_3NiSb_2O_9$. Here, the edge sharing isosceles triangles formed by the antiferromagnetically coupled Ni^{2+} ions along c axis may be involved with the observed glassy magnetic behavior, which is driven by the topological magnetic frustration.

Another possibility of the occurrence of magnetic frustration is the NN and NNN interactions leading to the AFM and FM interactions, which have been classically addressed in the literature [4, 6, 37, 38, 39]. The occurrence of AFM and FM interactions of comparable strengths close to T_g may cause magnetic frustration leading to the SG behavior. Figure 8(c) depicts an example of NN, NNN (or second NN), and third NN arrangements of Ni atoms. Here, NN, NNN, and third NN Ni−Ni distances are 3.9816/3.9830 Å, and 5.6341/5.6215 Å, and 6.8821 Å at 8.3 K, as shown in Fig. 8(c). These quantitative estimations of the Ni−Ni distances provide important clues for the possible AFM and FM exchange interactions. The sharp changes of Ni−O−Ni bond angles in the basal plane and along the apex are also directive, where apex bond angle approaches toward 180^0 and bond angle decreases significantly from 180^0 in the basal plane. These parameters are important for proposing possible AFM and FM interactions for interpreting magnetic frustration theoretically [40]. The possible magnetic structure, as determined from the neutron diffraction studies are proposed to establish origin of magnetic frustration in $Sr_3NiSb_2O_9$.

In conclusion, current study confirms spin-glass like transition in $Sr_3NiSb_2O_9$, as obtained from the low-field memory experiment at low temperature using dc magnetometry and frequency dependent ac susceptibility measurements. The synchrotron diffraction studies corroborate magnetoelastic coupling around $\sim$ 225 K and at the SG transition temperature. Nearly step-like anomalous and anisotropic lattice contraction close to T_g are observed and proposed to be correlated with the occurrence of magnetic frustration in the current investigation. Edge sharing isosceles triangular lattice arrangements formed by the Ni atoms, and/or interplay between NN and NNN Ni−Ni interactions may cause magnetic frustration, leading to the spin-glass-like behavior. Magnetic structure, as determined by the neutron diffraction studies and *ab* initio calculations using atomic

coordinates, as obtained from the synchrotron diffraction studies are proposed to settle the issue on the occurrence of spin-glass ground state in $Sr_3NiSb_2O_9$.

Acknowledgment

S.G. acknowledges the SERB project no. SB/S2/CMP-029/2014 and DST, India for the financial support (Proposal No.: I-20170178) to perform experiment at PETRA III, Hamburg, Germany for synchrotron diffraction studies. A.C. wishes to thank for the UGC fellowship.

References

[1] D.L.Stein and C.M.Newman *Spin Glasses and Complexity, Primers in Complex Systems* (Princeton University Press, Princeton, NJ, 2013).

[2] A. K. Bera and S. M. Yusuf, Phys. Rev. B 86 (2012) 024408.

[3] D. De, S. Majumdar, and S. Giri, J. Magn. Magn. Mater 394 (2015) 448-453.

[4] J. A. Mydosh, *Spin Glasses: An Experimental Introduction* (Taylor & Francis, London, 1993).

[5] S. F. Edwards and P. W. Anderson, J. Phys. F: Metal Phys. 5 (1975) 965 .

[6] K. Binder and A. P. Young, Rev. Modern Phys. 58 (1986) 801976.

[7] S. P. Muscinelli, W. Gerstner, and J. Brea, Neural Computation 29 (2017) 458.

[8] D. J. Amit, H. Gutfreund, H. Sompolinsky, Phys. Rev. A 32 (1985) 1007.

[9] R. Ballou, J. Alloys Compd. 275277 (1998) 510517.

[10] A. P. Ramirez, Annual Rev. Materials Science 24 (1994) 453-480.

[11] O. G. Ellert, A. V. Egorysheva, Yu. V. Maksimov, O. M. Gajtko, N. N. Efimov, R. D. Svetogorov, J. Alloys Compd. 688 (2016) 1-7.

[12] H. Shinaoka, Y. Tomita, and Y. Motome, Phys. Rev. Lett. 107 (2011) 047204.

[13] H. Shinaoka, Y. Tomita, and Y. Motome, J. Phys.: Conf. Ser. 400 (2012) 032087.

[14] H. Shinaoka, Y. Tomita, and Y. Motome, Phys. Rev. B 90 (2014) 165119.

[15] R. V. Aguilar, A. B. Sushkov, Y. J. Choi, S. -W. Cheong, and H. D. Drew, Phys. Rev. B 77 (2008) 092412.

[16] A. Kumar, S. D. Kaushik, V. Siruguri, and D. Pandey, Phys. Rev. B 97 (2018) 104402.

[17] J. Tejada, B. Martinez, A. Labarta, and E. M. Chudnovsky, Phys. Rev. B 44 (1991) 7698.

[18] P. D. Battle, C. -M. Chin, S. I. Evers, M. Westwood, J. Solid State Chem. 227 (2015) 1-4.

[19] P. D. Battle, S. I. Evers, E. C. Hunter, and M. Westwood, Inorg. Chem. 52 (2013) 66486653.

[20] K. Dey, A. Indra, D. De, S. Majumdar, and S. Giri, ACS Appl. Mater. Interfaces 8 (2016) 12901-12907.

[21] X. Bie, Y. Wei, L. Liu, K. Nikolowski, H. Ehrenberg, H. Chen, C. Wang, G. Chen, F. Du, J. Alloys Compd. 551 (2013) 3739.

[22] J. Strempfer, S. Francoual, D. Reuther, D. K. Shukla, A. Skaugen, H. Schulte-Schrepping, T. Kracht and H. Franz: Journal of Synchrotron Radiation 20 (2013) 541-549.

[23] C. P. Bean and J. D. Livingston, J. Appl. Phys. 30 (1959) S120.

[24] D. De, A. Karmakar, M. K. Bhunia, A. Bhaumik, S. Majumdar, and S. Giri, J. Appl. Phys. 111 (2012) 033919.

[25] M. T. Azcondo, J. R. Paz, K. Boulahya, C. Ritter, F. G. Alvarado, U. Amador, Dalton Trans. 44 (2015) 3801.

[26] X. Chen, S. Bedanta, O. Petracic, W. Kleemann, S. Sahoo, S. Cardoso, and P. P. Freitas, Phys. Rev. B 72 (2005) 214436.

[27] Y. Sun, M. B. Salamon, K. Garnier, and R. S. Averback, Phys. Rev. Lett. 91 (2003) 167206.

[28] M. Thakur, M. Pal Chowdhury, S. Majumdar, and S. Giri, Nanotechnology 19 (2008) 045706.

[29] K. Jonason, E. Vincent, J. Hammann, J. P. Bouchaud, and P. Nordblad, Phys. Rev. Lett. 81 (1998) 3243.

[30] S. Chakraverty, M. Bandyopadhyay, S. Chatterjee, S. Dattagupta, A. Frydman, S. Sengupta, and P. A. Sreeram, Phys. Rev. B 71 (2005) 054401.

[31] D. S. Fisher and D. A. Huse, Phys. Rev. Lett. 56 (1986) 1601.

[32] S. Pakhira, C. Mazumdar, R. Ranganathan, S. Giri, J. Alloys Compd. 742 (2018) 391-401.

[33] O. G. Ellert, A. V. Egorysheva, O. M. Gajtko, D. I. Kirdyankin, R. D. Svetogorov, J. Magn. Magn. Mater. 463 (2018) 1318.

[34] F. Lefloch, J. Hammann, M. Ocio, and E. Vincent, Europhys. Lett. 18 (1992) 647.

[35] J. E. Greedan, J. Mater. Chem. 11 (2001) 37.

[36] S. T. Bramwell, S. G. Carling, C. J. Harding, K. D. M. Harris, B. M. Kariuki, L. Nixon, and I. P. Parkin, J. Phys.: Condens. Matter 8 (1996) L123.

[37] S. T. Bramwell and M. J. P. Gingras, Science 294 (2001) 1495.

[38] K. Binder, Phys. Rev. Lett. 45 (1980) 811.

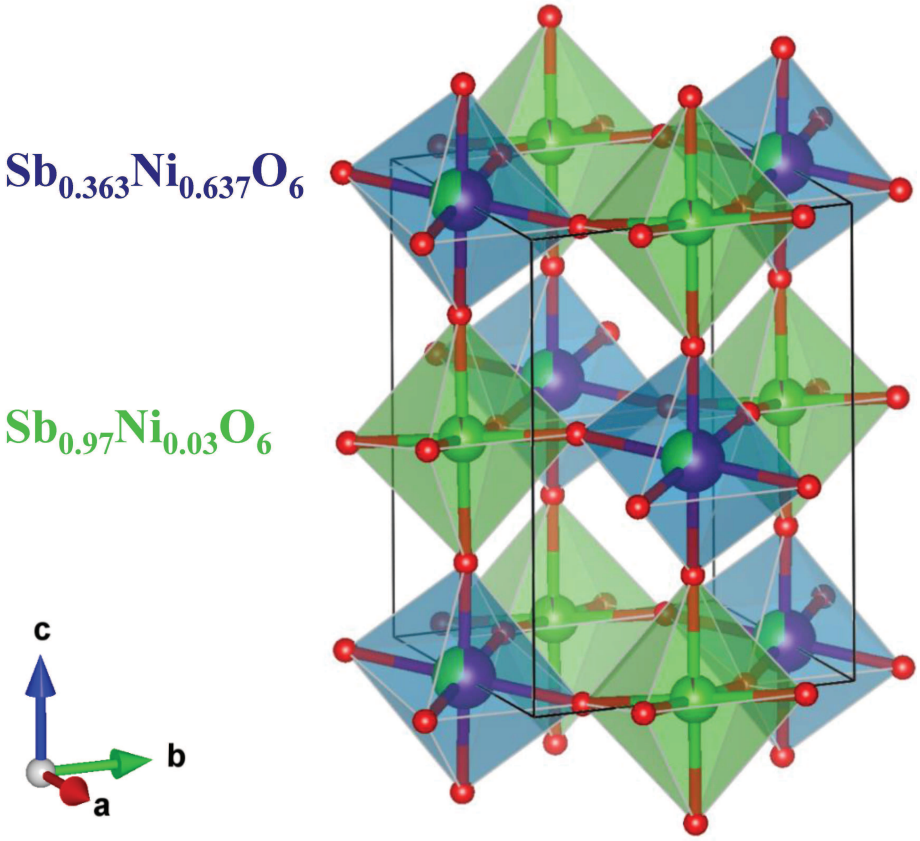

Figure 1: (Color online) The linkage of the $(Ni/Sb)O_6$ octahedra within the unit cell along with the fraction of atomic positions of Ni and Sb.

[39] R. N. Bhatt and A. P. Young, Phys. Rev. Lett. 54 (1985) 924.

[40] J. B. Goodenough and J. -S. Zhou, (2001). *Structure and Bonding* (Springer-Verlag Berlin Heidelberg, 2001).

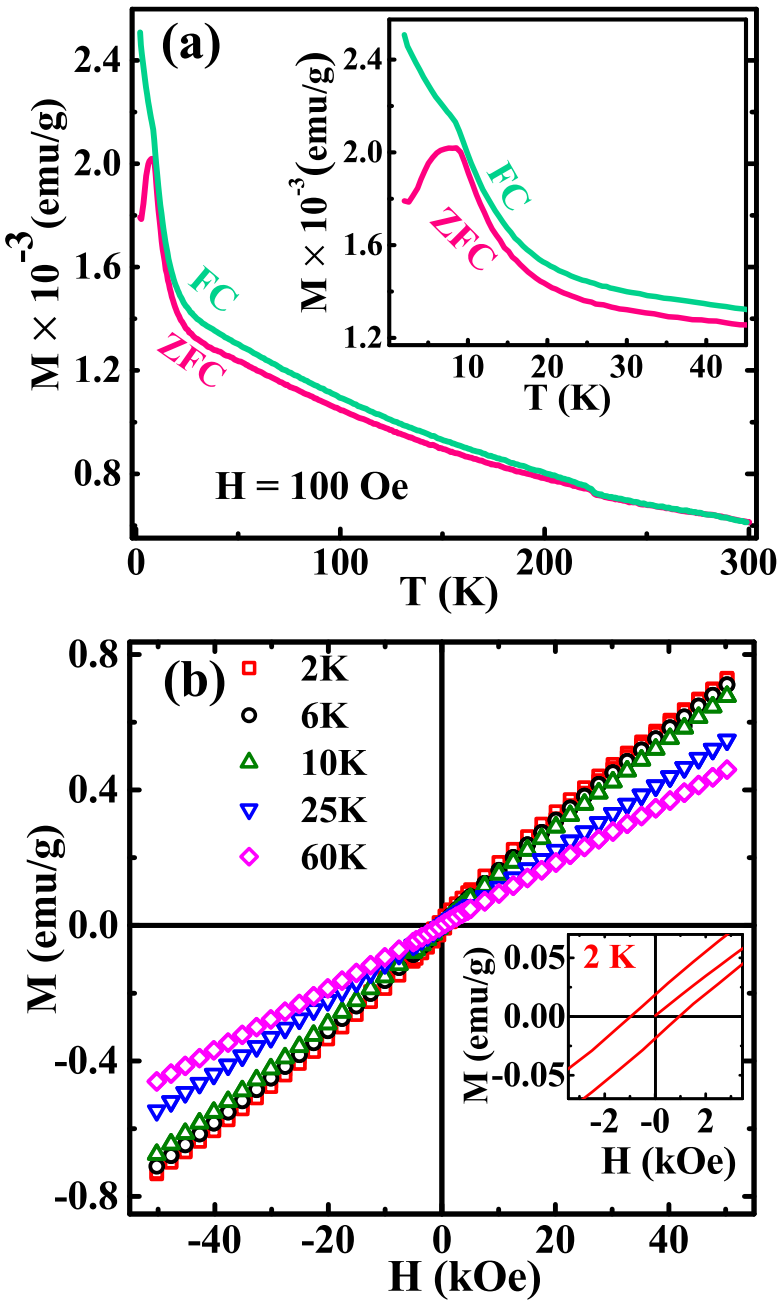

Figure 2: (Color online) (a) The T variations of ZFC and FC magnetization curves. Inset highlights the peak region. (b) Magnetic hysteresis loops recorded at selective temperatures. Inset shows central portion of the loop at 2 K.

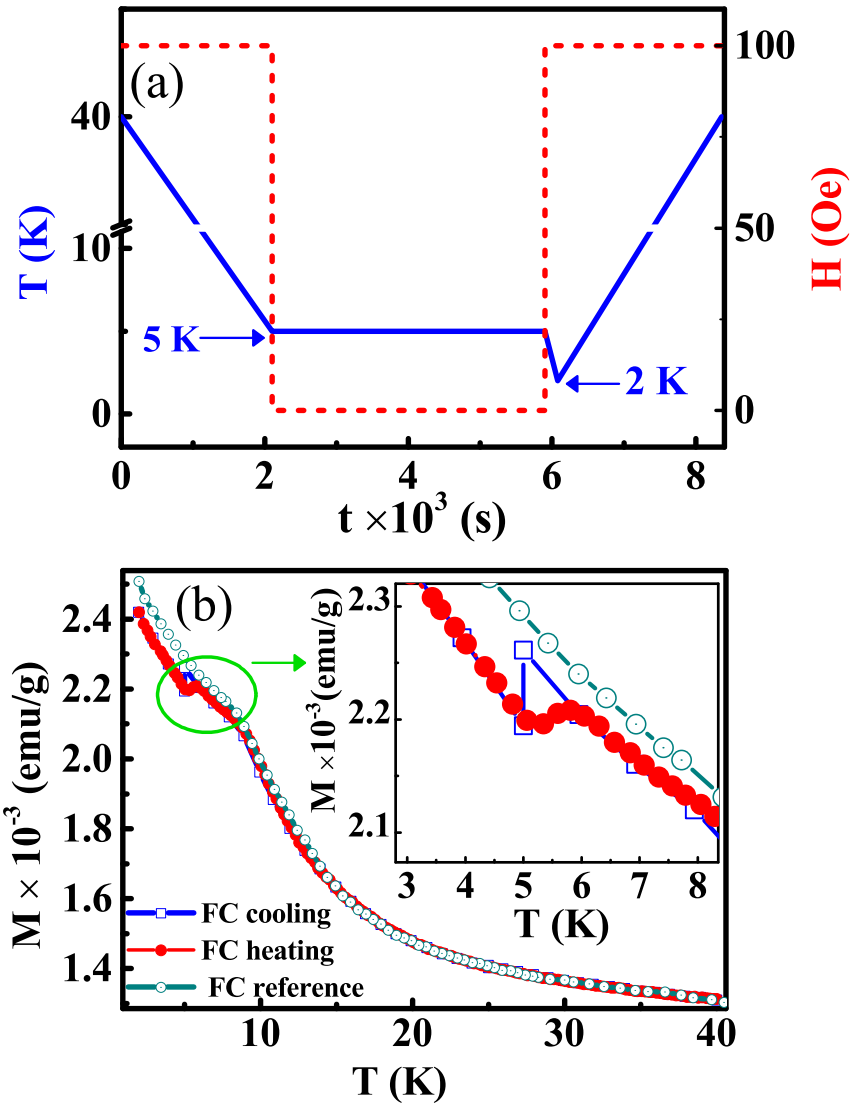

Figure 3: (a) The experimental protocols of memory effect in field-cooled mode are described. (b) The T variation of field-cooled (FC) magnetization in different modes. The field is cut off temporarily at 5 K. The FC cooling, FC heating, and FC reference curves are shown. Memory effect is demonstrated by the step at 5 K in the FC heating curve. Inset highlights the region around 5 K.

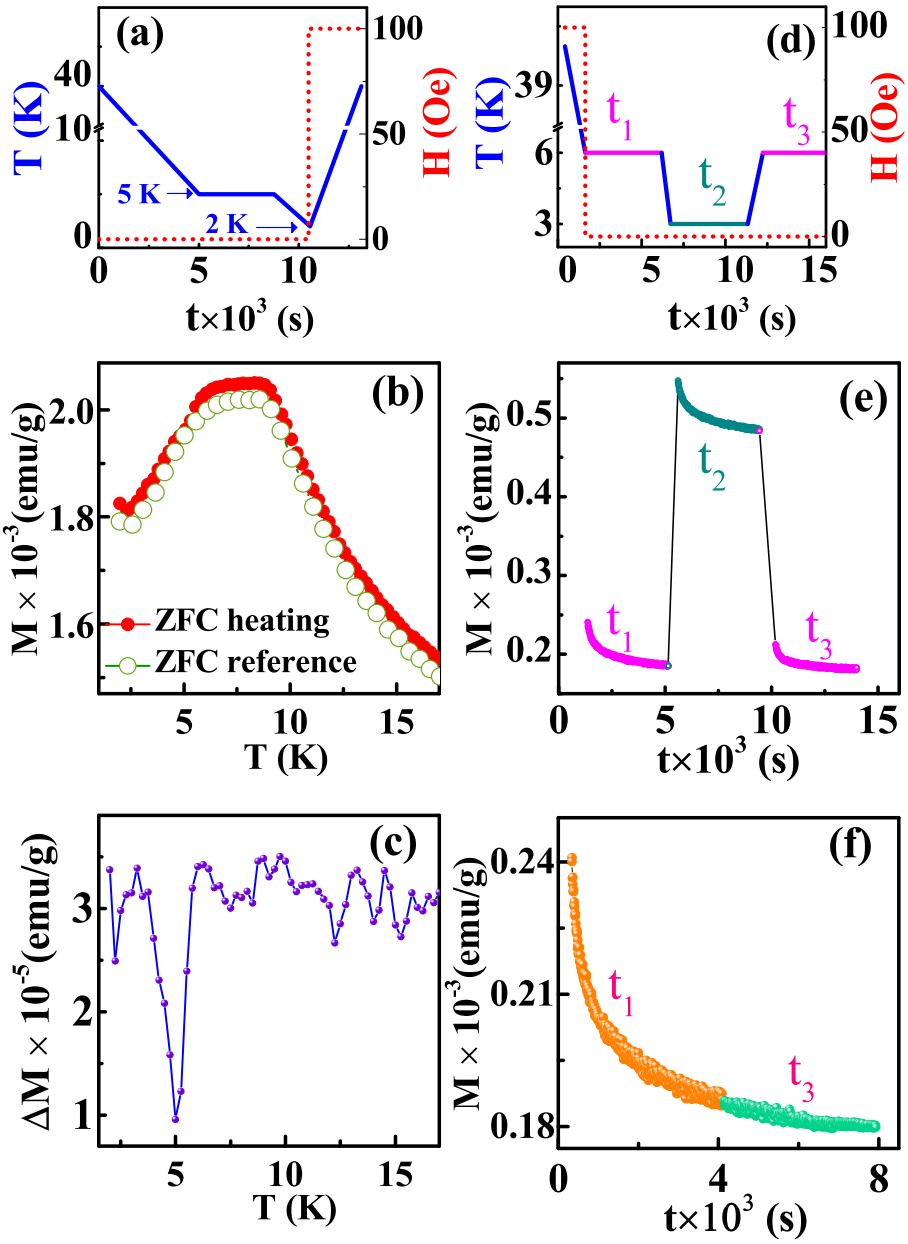

Figure 4: (Color online) (a) Experimental protocols of ZFC memory experiment are described. (b) ZFC heating and ZFC reference curves are shown, where sample temperature is halted at 5 K during cooling process in ZFC mode. (c) The difference plot (ΔM) with T. (d) Experimental protocols of relaxation memory experiment are described. (e) Magnetic relaxation in zero-field for t_1, t_2, and t_3 at 6 K, 3 K, and 6 K, respectively. (f) Plot of magnetic relaxation for t_1 and t_3 together displaying a single relaxation process at 6 K.

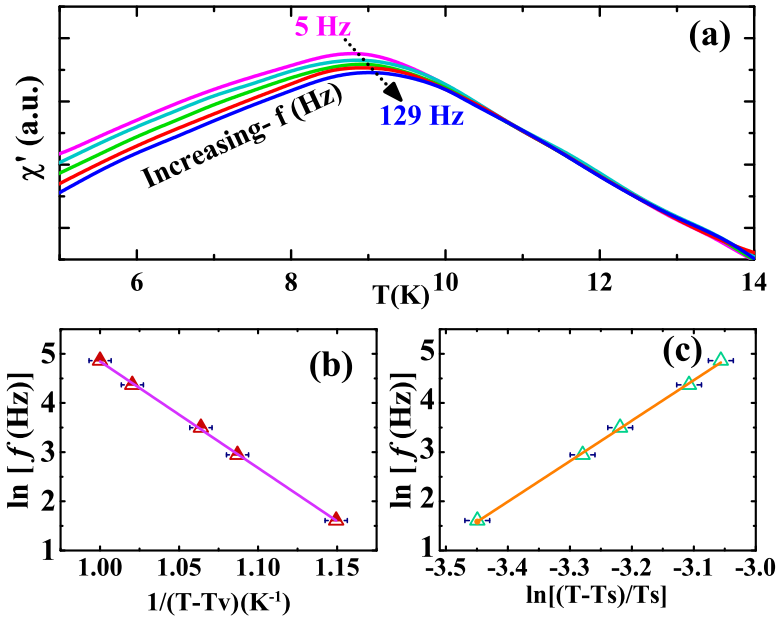

Figure 5: (Color online) (a) The T variation of χ' at different f. Verification of peak-shift with f followed by (b) Vogel-Fulcher law and (c) dynamical scaling law.

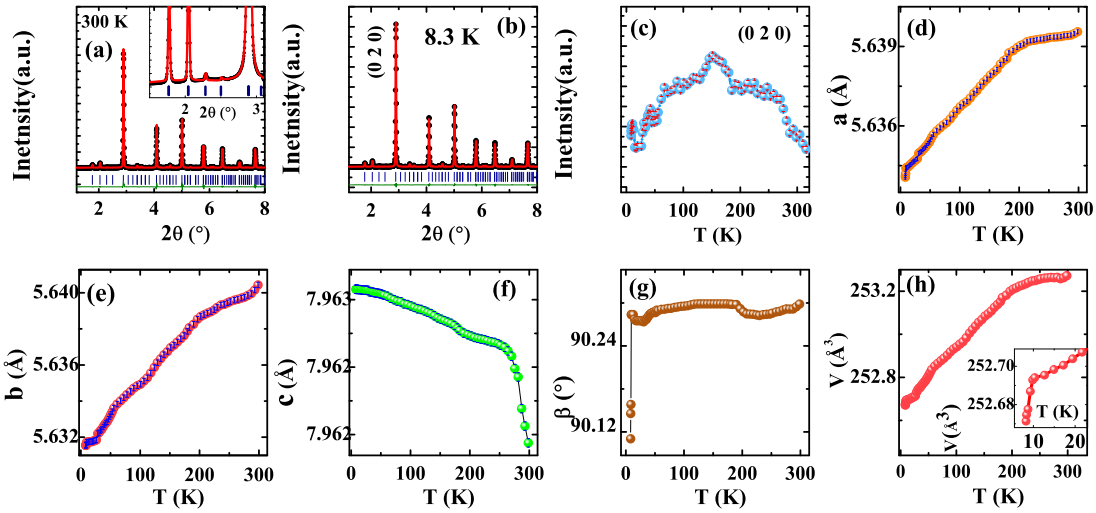

Figure 6: (Color online) Synchrotron diffraction patterns at (a) 300 K and (b) 8.3 K of $Sr_3NiSb_2O_9$. Inset of (a) demonstrates close view of a portion of the diffraction pattern. Continuous curves in (a) and (b) show the fit using Rietveld refinement. The T vairations of (c) intensity of the (110) peak, (d) lattice constant, a, (e) lattice constant, b, (f) lattice constant, c, (g) angle, β, and (h) unit cell volume, V. Inset of (h) highlights the low temperature region.

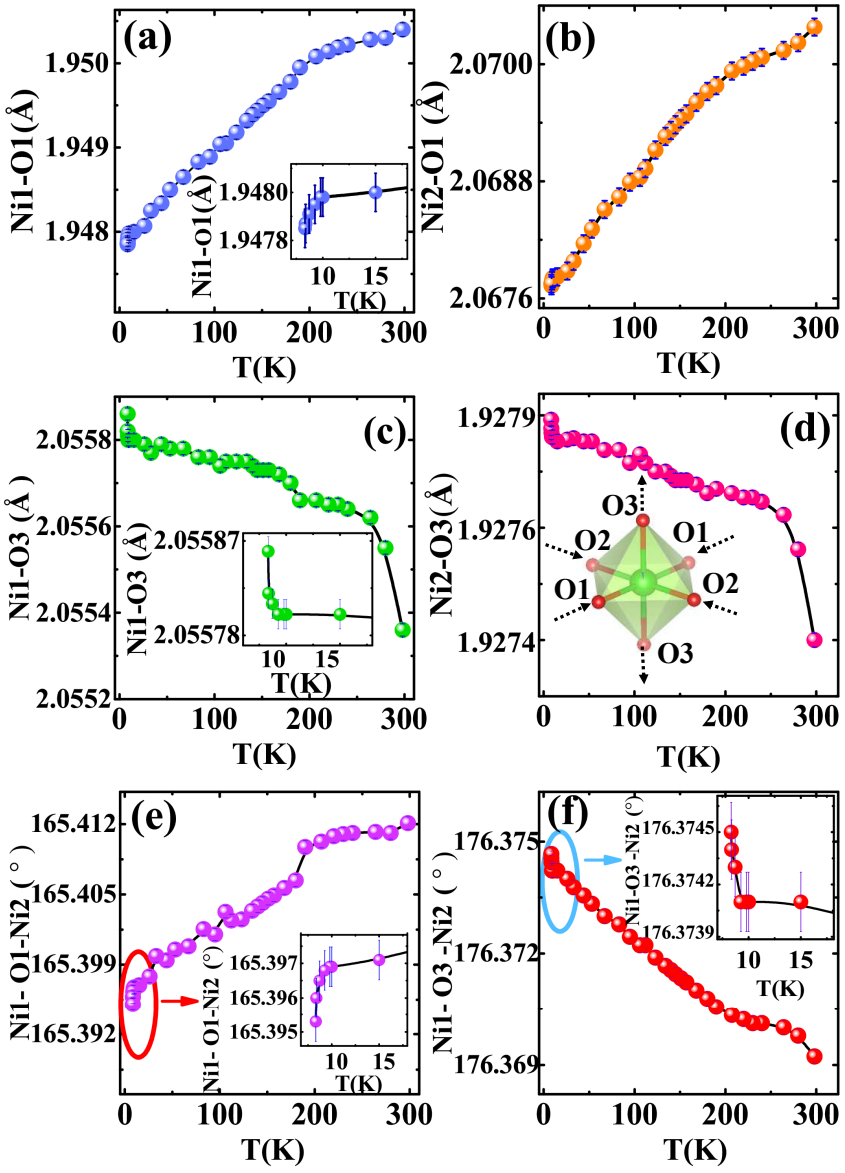

Figure 7: (Color online) The T variations of (a) Ni1−O1 bond length, (b) Ni2−O1 bond length, (c) Ni1−O3 bond length, (d) Ni2−O3 bond length, (e) Ni1−O1−Ni2 bond angle, and (f) Ni1−O3−Ni2 bond angle.

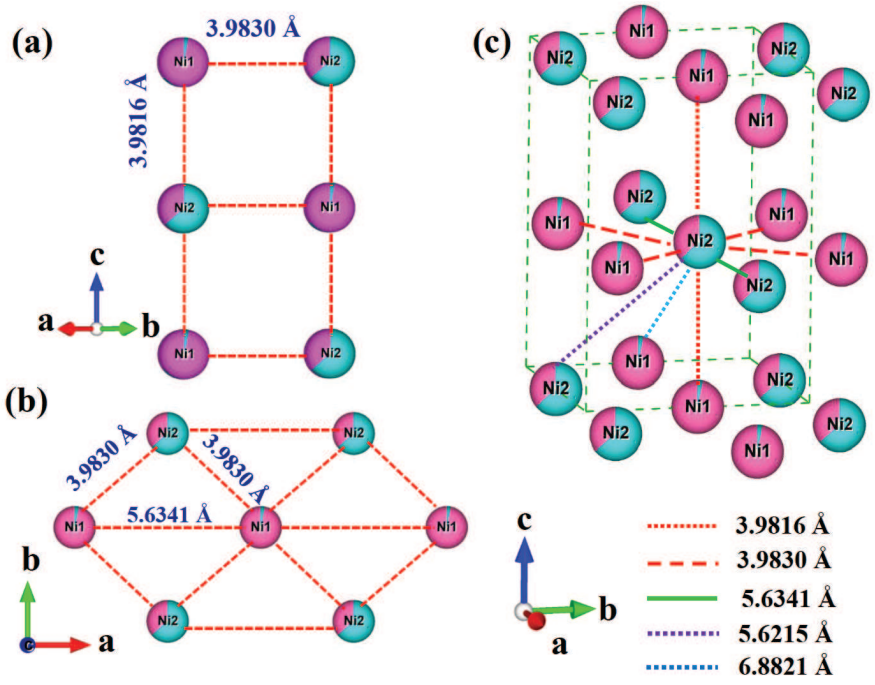

Figure 8: (Color online) The Ni atomic positions along different directions displaying (a) square lattice, (b) isosceles triangular lattice arrangements, and three-dimensioan views showing NN and NNN Ni atomic distances.